Int. J. Multiphase Flow Vol. 19, No. 1, pp. 125–136, 1993
Printed in Great Britain.

0301-9322/93 $6.00 + 0.00

PERFORMANCE AND FLOW CHARACTERISTICS OF NOZZLES FOR INITIALLY SUBCOOLED HOT WATER (INFLUENCE OF TURBULENCE AND DECOMPRESSION RATE)

J. OHTA,[1] T. FUJII,[2] K. AKAGAWA[3] and N. TAKENAKA[2]

[1]Department of Mechanical Engineering, Fukui University, 3-9-1, Bunkyo, Fukui 910, Japan

[2]Department of Mechanical Engineering, Kobe University, Rokkodai, Nada-ku, Kobe 657, Japan

[3]Department of Mechanical and System Engineering, Ryukoku University, 1-5, Yokotani, Seta, Otsu 520-21, Japan

(Received 2 July 1991; in revised form 26 October 1992)

Abstract—The purpose of this study was to improve the performance characteristics of a convergent–divergent nozzle for flashing expansion of initially subcooled hot water. The slip between the vapor and liquid along the divergent passage and the maximum nonequilibrium pressure drop at the nozzle throat (this is related to the thermal nonequilibrium) cause a decline in the nozzle efficiency. To decrease the maximum pressure drop, a nozzle with thin wires just upstream of the throat and a nozzle with a smaller convergent angle were manufactured and tested. Initially subcooled hot water at an inlet pressure of 0.47 MPa and inlet temperatures of 409.9 to 421.8 K (inlet subcoolings of 0.9–12.9 K) were used with the nozzle back pressures ranging from 5 to 101.3 kPa. The following results were attained: (1) the maximum nonequilibrium pressure drop at the throat decreased and the thrust coefficient increased by 10%; (2) the thrust coefficient was found to be independent of the inlet subcooling and exit stream-expansion ratio; (3) a correlation between the ratio of the exit pressure to the inlet pressure and the appropriate exit stream-expansion ratio was obtained empirically; and (4) the critical flow rate was found to be lower than that for an ordinary convergent–divergent nozzle.

Key Words: flashing, critical flow rate, thrust coefficient, convergent–divergent nozzle, decompression rate, pressure undershoot

1. INTRODUCTION

From the viewpoint of utilization of water-dominated geothermal resources or waste heat from factories, it is necessary to develop an efficient energy conversion device which can convert the thermal energy of subcooled hot water or a low-quality steam–water mixture into power. One such device which has been proposed is a total flow turbine, i.e. a two-phase flow turbine (Austine *et al.* 1973). Recently, Akagawa *et al.* (1988a) analyzed the performance of total flow turbine systems, including two-phase flow turbines and a flash-steam turbine. As a result, it was shown that the overall efficiency of the total flow turbine system depends on the two-phase flow turbine efficiency. Furthermore, another report (Akagawa *et al.* 1984) clarified that it is most important to develop a highly efficient two-phase flow nozzle when adopting a turbo-type of machine as the two-phase flow turbine.

When the thermal energy of hot water or a low-quality steam–water mixture is converted into kinetic energy through a nozzle, a decompression flashing and a critical phenomenon occur. As for the two-phase flow in the nozzles, there have been a number of investigations (Schrock *et al.* 1977) on choked two-phase flow in relation to the hypothetical "loss of coolant accident". In these experiments, long ducts, short ducts, nozzles with various divergent angles and nozzles with various throat diameters were used to investigate the effects of the inlet subcooling and inlet quality on the critical mass flow rates. In the analysis, the critical mass flow rates and pressure profiles were calculated from: a two-fluid flow model taking the slip between the vapor and liquid into account (Moody 1966; Levy 1965); a model which considers thermal nonequilibrium assuming equal velocity of the vapor and the liquid; and a two-fluid model which takes both the thermal nonequilibrium and the slip into account (Ardron 1978; Richter 1983). Wallis (1980) and Isbin (1980) presented overviews of the critical flow rate. Moreover, to investigate the role of

the crystal. The shape of the drop was noted until no further change could be observed; the time for stabilization was sometimes instantaneous and sometimes several hours or a day. The angle through the water phase was estimated by eye to within 10°, and the system was categorized as water-wet, 0–70°; intermediate, 80–100°; or oil-wet, 110–180°. Some of these experiments were also performed in the reverse orientation with a drop of dodecane placed below a crystal suspended in an aqueous solution of the adsorbate. No significant differences were observed between the two methods.

3. Adsorption results

3.1. TGA *method and analysis*

Thermogravimetric analyses (TGA's) were run on powdered samples of carbonates after they had been treated with a solution of the organic adsorbate. The weight of the sample was followed as it was heated, and a weight loss was measured when the organic left the sample. Both qualitative and quantitative information was gained. The temperature of the weight loss indicated how strongly the adsorbate was bound to the surface. Low-temperature losses (below 250°C) indicated volatilization (desorption) of the organic without the disruption of any chemical (intramolecular) bonds. High-temperature weight losses occurred when the organic molecule combusted or decomposed before it desorbed from the surface. Low-temperature weight losses indicated a weak, physical adsorption, and high-temperature weight losses indicated a strong, chemical or ionic adsorption. From the magnitude of the weight losses, we quantified the amount of organic material on the surface.

The magnitude of the TGA weight loss can be used to calculate the extent of surface coverage. From table 1 of Thomas and Clouse (1989), we calculate for calcite an average surface area per calcium ion of 20.8 $Å^2$. This very closely matches the 20.5 $Å^2$ per molecule that is generally used for close-packed fatty-acid molecules oriented perpendicularly to a surface. If we assume that the adsorbates interact with calcium ions on a one-to-one basis, the calcium ion spacing will determine the adsorbate packing for fatty acids and other adsorbates with a head group size of $\leqslant 20.8$ $Å^2$. This yields a theoretical monolayer coverage of 8.0 μmol m^{-2} for calcite. Theoretical coverage for dolomite was obtained with the equation:

$$(\text{dolomite coverage}) = (\text{calcite coverage}) \left[\frac{(\text{dolomite volume})}{(\text{calcite volume})} \right]^{2/3}$$

Magnesite coverage was calculated similarly. This gave theoretical coverages 8.9 and 10.0 μmol m^{-2} for dolomite and magnesite, respectively.

We were also able to test the reversibility of the adsorption with the TGA. Some samples were washed with solvent following adsorption, and TGA's were run to see if the adsorbate remained on the surface. Adsorbates fell into two classes. The first class we call easy-to-reverse adsorbates; these were washed off by any solvent we tried (heptane, isopropanol, or water). The second class we call difficult-to-reverse adsorbates. These were not washed off by heptane or water but could be removed by alcohols and by hydrocarbon–water mixtures.

3.2. Comparison to other methods

The objective of this work was to determine the types of organic compounds that adsorb on carbonates and the strength of that adsorption. TGA measurements provide a direct measurement of surface concentration and strength of adsorption. Solution concentrations and volumes were ample to provide monolayer coverage, but they were not routinely measured to provide a detailed understanding of the relationship between adsorption and solution concentration. The reasons for this omission are

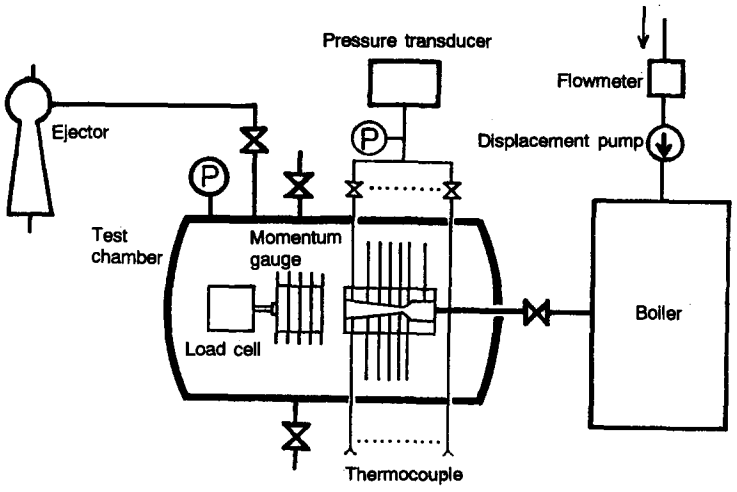

Figure. 1. Schematic diagram of the experimental apparatus.

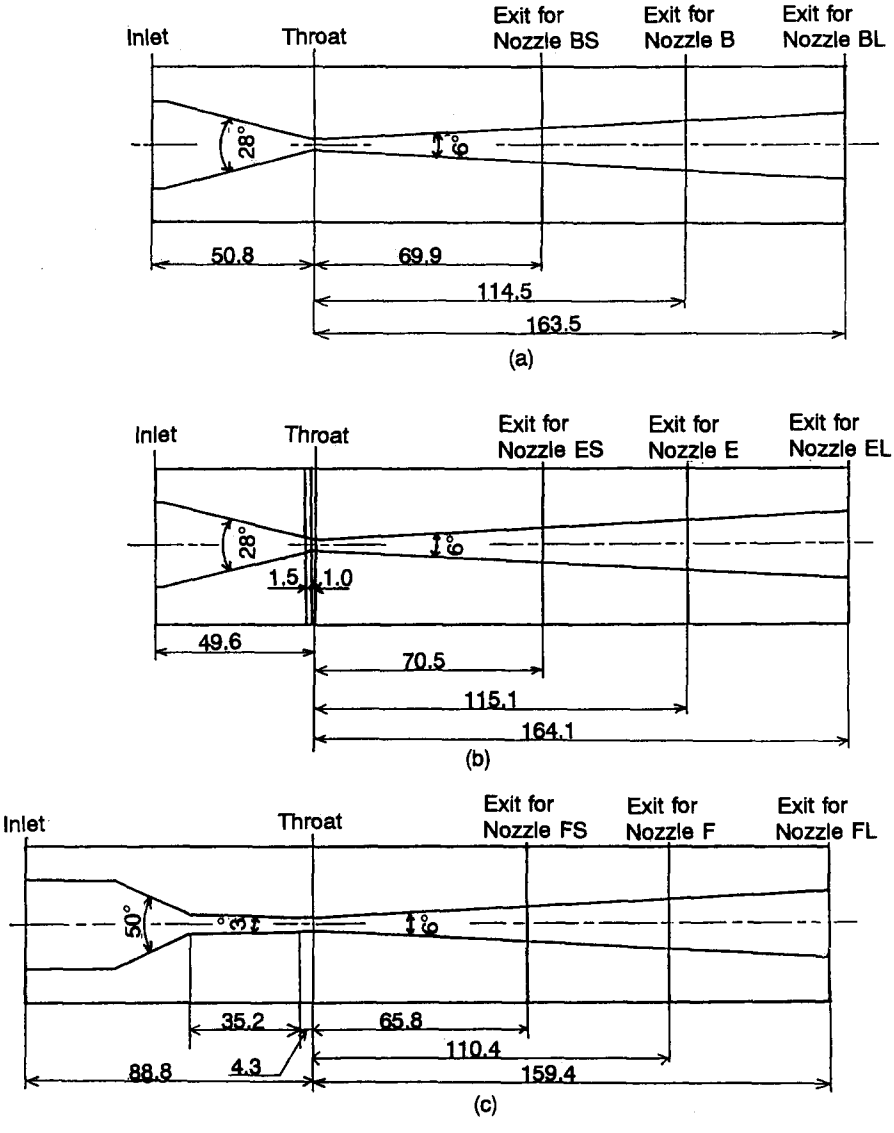

Figure 2(A). Cross sections of the nozzles.

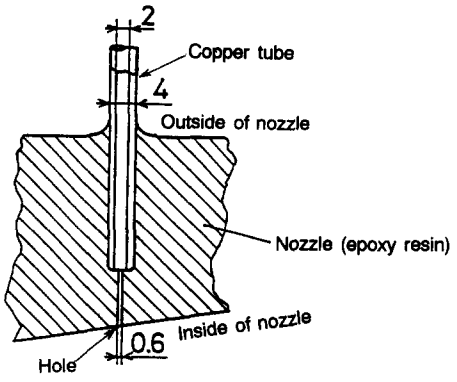

Figure. 2(B). Cross section near a pressure tap.

pressure undershoot. According to the relationship that the pressure undershoot decreases with decreasing decompression rate, the convergent angles of nozzles FS, F and FL were set low in order to achieve a low maximum nonequilibrium pressure drop at the throat. That is, nozzles FS, F and FL all had the same convergent passage configuration, such that the convergent angles were 0°, 3° and 50° along the axial distances of 0–4.3, 4.3–39.5 and 39.5–62.4 mm upstream of the throat, respectively.

Since a once-through boiler was used in this experiment, the mass flow rate to the boiler is the same as that for nozzles. Thus, the mass flow rate for the nozzles was measured upstream of the boiler using the integrated flowmeter. To obtain the desired pressure and temperature of the subcooled hot water at the inlet the authors repeatedly adjusted the flow rate and heat input to the boiler like a numerical iteration. In this sense, the inlet temperature and pressure are independent variables of the experiments and the flow rate is a dependent variable. The inlet pressure was 0.47 MPa and the inlet temperatures were 409.8–411.9, 415.6–417.1 and 420.7–421.8 K.

The static pressure profiles along the nozzle axis were measured through pressure taps in the wall. As can be seen in a cross section of the pressure tap in detail [figure 2(B)], the hole of 0.6 mm dia was connected to a copper tube and this tube was connected to a pressure transducer. The pressure was detected by the pressure transducer and was recorded via an amplifier. The number of pressure taps is given in table 1.

The temperature was measured at the inlet cross section of the nozzle by a chromel–alumel thermocouple of 0.1 mm dia. The thrust of the two-phase mixture jet was measured by a load cell connected to a momentum gauge, consisting of wire meshes of different sizes to absorb the two-phase mixture jet. The load cell was cooled by a water jacket.

The accuracy of the measured thrust coefficient may be subject to some errors. Since the thrust coefficient is defined in [6], the accuracy is subject to errors in the thrust, flow rate and adiabatic heat drop. The adiabatic heat drop was calculated based on the measured pressure and temperature at the nozzle inlet and the back pressure. Thus, the overall accuracy was estimated from measurements of the thrust, flow rate, inlet pressure, inlet temperature and back pressure. The uncertainty in the flow rate is within $\pm 2\%$ of the measured value in the range of the measurements. The thrust was measured within $\pm 2\%$. The uncertainty in the pressure is within $\pm 1\%$ and the

Table 1. Nozzle specifications

	Nozzles								
	BS	B	BL	ES	E	EL	FS	F	FL
Convergent angle (deg)	28	28	28	28	28	28	3	3	3
Divergent angle (deg)	6	6	6	6	6	6	6	6	6
Throat dia (mm)	3.5	3.5	3.5	3.5	3.5	3.5	4.0	4.0	4.0
Nozzle exit dia (mm)	10.0	15.4	20.0	10.8	15.4	20.0	10.6	15.4	20.0
Length of the divergent passage (mm)	69.9	114.5	163.5	70.5	115.1	164.1	65.8	110.4	159.4
Exit stream-expansion ratio	9.5	19.4	32.7	9.5	19.4	32.7	7.3	14.8	25.0
No. of pressure taps along the passage	12	14	16	12	14	16	12	14	16

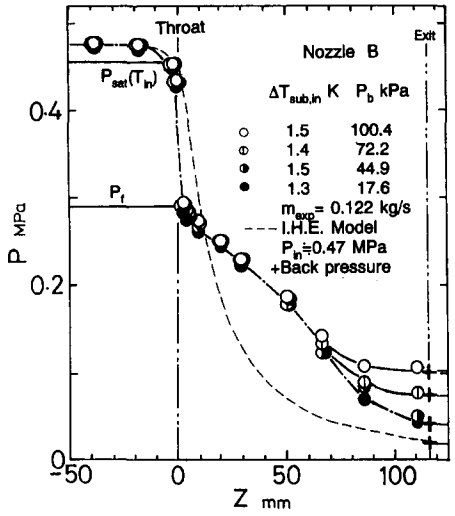

Figure 3. Axial pressure profiles for a conventional nozzle.

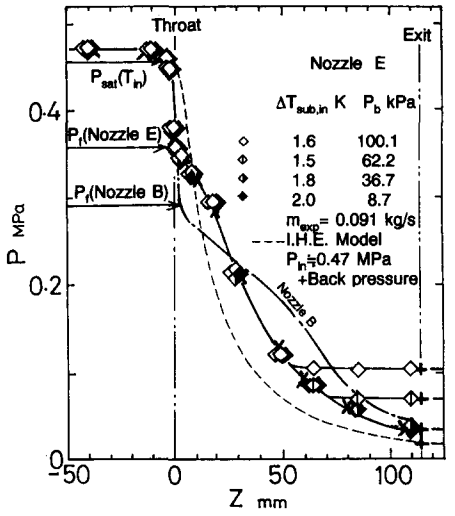

Figure 4. Pressure profiles of the nozzle with thin wires installed.

temperature was measured within $\pm 0.5\%$. The overall uncertainty in the thrust coefficient was estimated to be within $\pm 5\%$. The uncertainty in the critical flow rate is subject to the measured mass flow rate and the cross-sectional area measured at the nozzle throat. The overall uncertainty in the critical flow rate was estimated to be $\pm 4\%$.

3. EXPERIMENTAL RESULTS AND DISCUSSIONS

3.1. Optimum pressure profile

In figure 3, pressure profiles for nozzle B were plotted against the axial distance from the nozzle throat z (the axial distance is positive downstream of the throat) under the conditions of an inlet pressure of 0.47 MPa, inlet subcoolings of 1.3–1.5 K and back pressures of 17.6, 44.9, 72.2 and 100.4 kPa. It can be seen that the axial pressure profile changes with the back pressure above back pressures of 40 kPa and that the axial pressure profile in the nozzle does not change below back pressures of 40 kPa. The pressure profile which was not affected by the back pressure was denoted as an optimum pressure profile and the back pressure as an optimum back pressure in the authors' study (Akagawa *et al.* 1988b). In figure 3, a pressure profile calculated from the isentropic homogeneous equilibrium model (IHE model) is also shown (by the dashed line) for the same inlet conditions. In the calculation, the pressure at the nozzle throat is equal to the saturation pressure corresponding to the inlet temperature and flashing takes place at the throat above inlet subcooling of 1 K. Comparing the measured pressure profile with the calculated one, it was estimated that flashing occurs near the divergent side of the nozzle throat. A pressure difference between the saturation pressure and P_f [shown as $P_{sat}(T_{in}) - P_f$ in figure 3] is denoted as the maximum nonequilibrium pressure drop at the throat in this paper. In general, the degree of thermal nonequilibrium decreases as the maximum nonequilibrium pressure drop at the throat decreases. Thus, the maximum nonequilibrium pressure drop at the throat appears to be related to the degree of thermal nonequilibrium.

3.2. Effect of thin wires installed near the throat on the pressure profile

In figure 4,† pressure profiles for nozzle E (thin wires installed in a nozzle with the same configuration as nozzle B) are shown for an inlet pressure of 0.47 MPa, inlet subcoolings of 1.5–2.0 K and back pressures of 8.7, 36.7, 62.2 and 100.1 kPa. The optimum pressure profile for

†A direct current of 35 mA at 100 V was supplied between the two thin wires in nozzle E and observations confirmed that hydrogen bubbles were generated in a preliminary test. In this case the pressure profile is also shown using the symbols × in figure 4. However, it was noticed that the pressure profile did not differ from that without the current and the critical flow rate was not influenced by the current.

nozzle B is shown by the dashed line for comparison. As can be seen from the figure, an optimum pressure profile (shown by the solid line) exists for nozzle E which differs from that for nozzle B (shown by the dash/dot line) and the maximum nonequilibrium pressure drop at the throat for nozzle E was also lower than that for nozzle B. This can be considered to be due to the fact that the disturbance caused by the thin wires stimulates a flashing inception, thereby shortening the delay time for the vapor formation.

In figure 5, the pressure profiles measured for nozzles B and E and the pressure profile calculated from the IHE model are plotted against the dimensionless cross-sectional area ratio based on the throat (A/A_t), with the inlet subcooling as the parameter. It was concluded that the installation of thin wires in this manner can lower the maximum nonequilibrium pressure drop at the throat and change the optimum pressure profile. It is shown that for inlet subcooling $\Delta T_{sub,in} = 1$ K, the measured pressure ratios P/P_t are higher than the value calculated by the IHE model for the same cross-sectional area ratio above $A/A_t = 6$; and for $\Delta T_{sub,in} = 11$ K, the measured pressure ratios are smaller than the calculated ones. The reason may be that the higher measured pressure profiles are primarily caused by a larger mass flow rate (m) than that of the IHE model, for $\Delta T_{sub,in} = 1$ K ($m = A_t G_c = 0.25\pi d^2 G_c = 0.051$ kg/s, where A_t is the cross-sectional area based on the throat and G_c is the critical flow rate) and $\Delta T_{sub,in} = 11$ K the lower measured pressure profile is mainly caused by a larger velocity ratio, in spite of the fact that the measured mass flow rate is almost equal to that of the IHE model ($m = A_t G_c = 0.25\pi d^2 G_c = 0.143$ kg/s).

3.3. *Effect of the convergent angle on the pressure profiles*

Pressure profiles measured for nozzle F, which has a convergent angle of 3°, are shown by a solid line in figure 6 under an inlet pressure of 0.47 MPa, inlet subcoolings of 1.5–1.6 K and various back pressures in the range 20.3–100.8 kPa. In figure 6, the optimum pressure profile for nozzle B (convergent angle of 28°) in the divergent passage is shown as a dashed line. As can be seen from the figure, an optimum pressure profile exists for nozzle F, which differs from that for nozzle B, and the magnitude of the maximum nonequilibrium pressure drop at the throat is lower than that in nozzle B. Figure 6 also indicates that the measured pressure for nozzle F is lower than the pressure calculated using the IHE model upstream of the nozzle throat. One of the causes may be the fact that the mass flow rate for nozzle F is lower than that for the IHE model. Then, a pressure profile was calculated from Bernoulli's equation using a measured mass flow rate (for nozzle F) of 0.116 kg/s without flashing along the convergent passage. This pressure profile is shown by the dash/dot line and the pressure profile calculated from the IHE model with evaporation is shown by the dashed line in figure 7. From the IHE model, a mass flow rate results in $m = 0.0739$ kg/s and flashing occurs at the nozzle throat for $P_{in} = 0.47$ MPa and $\Delta T_{sub,in} = 1.5$ K. (1) It is shown

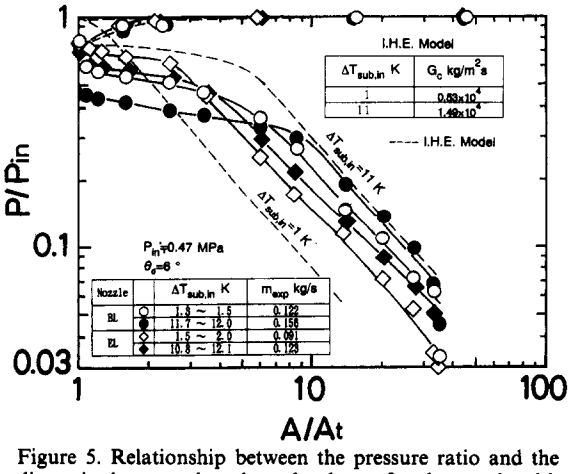

Figure 5. Relationship between the pressure ratio and the dimensionless area based on the throat for the nozzle with thin wires installed.

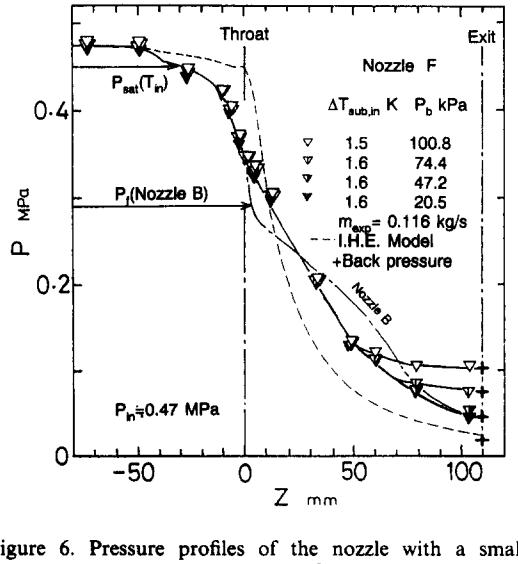

Figure 6. Pressure profiles of the nozzle with a small convergent angle.

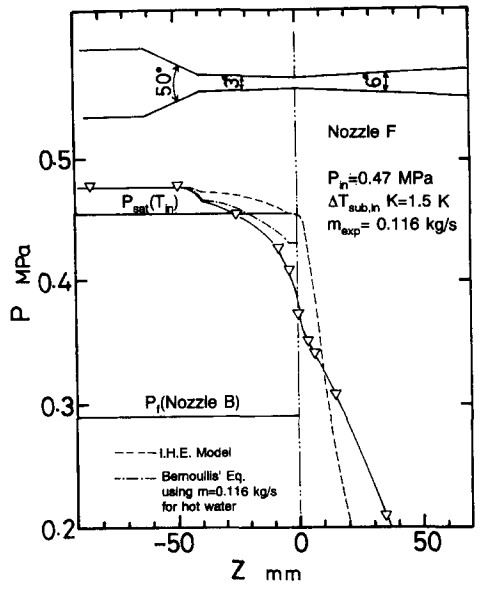

Figure 7. Comparison of the measured pressure profiles with calculated ones.

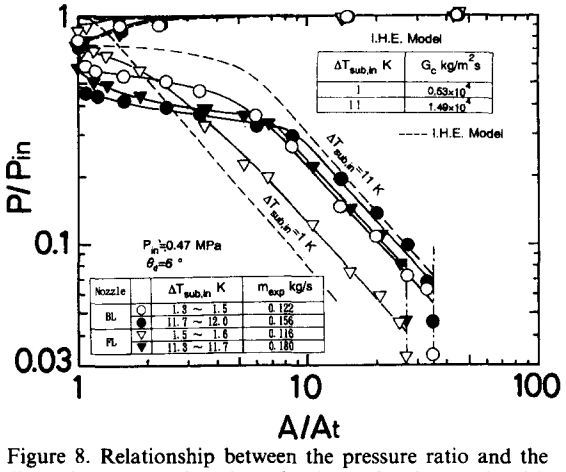

Figure 8. Relationship between the pressure ratio and the dimensionless area based on the throat for the nozzle with a small convergent angle.

that both the measured pressure and the calculated pressure (the dash/dot line) are lower than the saturation pressure corresponding to the inlet temperature in some part of the convergent passage. (2) As can be seen, the measured pressure decreases along the convergent passage ($z = -40$ to -8 mm) with a slight deviation from that calculated using $m = 0.116$ kg/s in the convergent passage. The deviation become larger near the throat ($z = -8$ to 0 mm). Thus, this suggested that flashing occurs in the region of $z = -8$ to 0 mm or upstream of $z = -8$ mm. The measured pressure would be approximately the same as that calculated using $m = 0.116$ kg/s, if flashing does not occur upstream of the throat. Figure 7 also indicates that a smaller convergent angle lowers the maximum nonequilibrium pressure drop at the throat.

The optimum pressure profiles for nozzles B and F and the pressure profile calculated from the IHE model were plotted against the cross-sectional area ratio, with inlet subcooling as the parameter, in figure 8. As can be seen from the figure, the optimum pressure profiles for nozzle F differ from those for nozzle B as mentioned above. The flashing inception upstream of the throat does not always cause the nozzle efficiency to increase, due to a large pressure loss in the convergent passage (as shown in figure 7). It was concluded that the convergent angle changes the optimum pressure profile and decreases the maximum nonequilibrium pressure drop at the throat.

3.4. Maximum nonequilibrium pressure drop at the throat

The maximum nonequilibrium pressure drop at the throat can be considered as one of the parameters for expressing the degree of thermal nonequilibrium. The maximum nonequilibrium pressure drops at the throat for nozzles BS, B, BL, ES, E and EL were read from the measured pressure profiles. These were plotted against the decompression rate, with inlet subcooling as the parameter, in figure 9. The decompression rates Σ were evaluated from [1] (Abuaf *et al.* 1983) by substituting the measured mass flow rates G_c and setting the unsteady term (the second term on the r.h.s.) to zero:

$$\Sigma = \frac{\partial P}{\partial z}\frac{\partial z}{\partial t} + \frac{\partial P}{\partial t} = \frac{G_c^3}{\rho^2}\frac{\mathrm{d}(\ln A)}{\mathrm{d}z} + \frac{\partial P}{\partial t}, \qquad [1]$$

where A, ρ and G_c are the cross-sectional area, liquid density and critical mass flow rate, respectively. It is shown in figure 9 that the maximum nonequilibrium pressure drop at the throat decreases with increasing inlet subcooling or a decreasing decompression rate. It is seen that the installation of wires plays an important role. Thus, it was confirmed that the installation of wires in this manner and decreasing the decompression rate are effective in lowering the maximum nonequilibrium pressure drop at the throat.

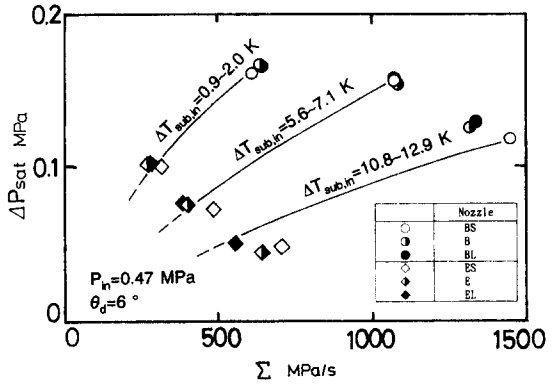

Figure 9. Maximum nonequilibrium pressure drop at the throat vs decompression rate.

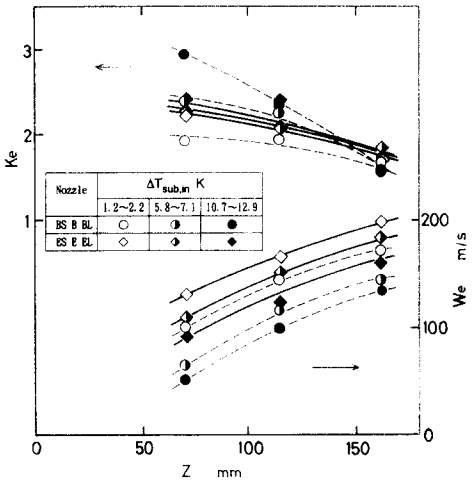

Figure 10. Velocity and liquid phase velocity.

Next, the velocity ratio and the critical flow rate are mentioned. These are important regarding the performance characteristics of nozzles.

3.5. *Velocity ratio, K*

Since the exit quality and velocity ratio could not be measured directly in these experiments, these values were estimated based on a separated flow model. The estimation method is as follows. Assuming that thermal equilibrium exists at the nozzle exit, the continuity, momentum and energy equations for the separated flow model can be expressed as follows:

$$m_{exp} = \frac{W_{L,e}}{v_{L,e}} \frac{1-\varepsilon_e}{1-x_e} = \frac{W_{G,e}}{v_{G,e}} \frac{\varepsilon_e}{x_e}, \quad [2]$$

$$F_{exp} = m_{exp}[(1-x_e)W_{L,e} + x_e W_{G,e}], \quad [3]$$

$$h_{in} - h_e = (1-x_e)\frac{W_{L,e}^2}{2} + x_e \frac{W_{G,e}^2}{2} \quad [4]$$

and

$$h_e = (1-x_e)h_{L,sat}(P_{ex}) + x_e h_{G,sat}(P_{ex}), \quad [5]$$

where x_e, ε_e, $W_{L,e}$, $W_{G,e}$, P_{ex}, h_e, $h_{L,sat}(P_{ex})$ and $h_{G,sat}(P_{ex})$ are the quality, void fraction, actual liquid velocity, actual gas velocity, pressure, specific enthalpy of the liquid at a given saturation pressure and specific enthalpy of the gas at a saturation pressure at the nozzle exit; h_{in} is the specific enthalpy of the liquid at the nozzle inlet. Substituting the measured values of the mass flow rate m_{exp}, thrust F_{exp}, inlet temperature and exit pressure P_{ex} into these equations, we can solve these simultaneous equations to obtain x_e, ε_e, $W_{L,e}$, and $W_{G,e}$. As mentioned in an author's paper, the optimum pressure profiles for nozzles BS and B overlapped upstream of that for nozzle BL. Thus, a curve which connects each experimental point (exit velocity ratios for nozzles BS, B and BL) can be considered to show the distribution of the velocity ratio approximately along the nozzle BL axis. These results for nozzles BL and EL are shown, with inlet subcooling as the parameter, in the upper part of figure 10. Liquid velocity profiles obtained in a similar way are also shown in the lower part of figure 10. It is shown that the velocity ratios decrease downstream and become 1.5–1.7 at $z = 165$ mm. As can be seen from the figure, in nozzle E, the influence of the inlet subcooling on the velocity ratio is smaller.

3.6. *Critical flow rate*

Measured critical flow rates are plotted against the inlet subcooling under an inlet pressure of 0.47 MPa for nozzles B, E and F in figure 11. The critical flow rates were calculated from the IHE, Henry–Fauske (Henry & Fauske 1971) and Abuaf [flow coefficient C_D is set to unity

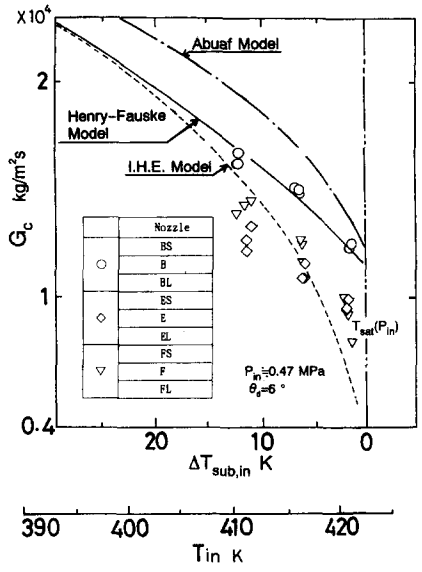

Figure 11. Critical flow rate.

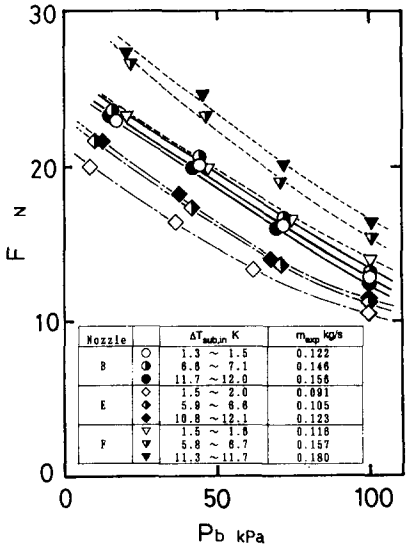

Figure 12. Thrust.

(Abuaf *et al.* 1983)] models and are also shown in figure 11. The measured G_c for nozzles E and F are lower than that for nozzle B by almost 30%. This can be explained as follows. The pressure difference for nozzles E and F between the inlet pressure and P_f (described in section 3.1) is lower than that for nozzle B due to a decrease in the maximum nonequilibrium pressure drop at the throat. If the pressure difference $(P_{in} - P_f)$ is related to (e.g. is approximately proportional to) the difference between the inlet pressure and the flashing inception pressure, Bernoulli's equation can be applied between the latter pressure difference (liquid alone flows in this region). Thus, the decrease in the critical flow rate with a decrease in the maximum nonequilibrium pressure drop at the throat appears reasonable.

Above an inlet subcooling of 10 K, the measured G_c are less than that for the IHE model. This is believed to be due to the fact that a boundary layer develops or flow separation occurs near the throat, since the liquid velocity near the flashing inception point increases with increasing inlet subcooling. Comparing the measured G_c with the G_c predicted by the Henry–Fauske and Abuaf models, these G_c have the same tendency. As can be seen from the fact that the measured G_c for nozzles E and F agree with the Abuaf model in the case of a flow coefficient of 0.7.

3.7. Thrust and the thrust coefficient

The thrust and the thrust coefficient are the important factors which affect the turbine output and the turbine efficiency. The experimental results of these factors are discussed in this section. The measured thrust for nozzles B, E and F are plotted against the back pressure, with inlet subcooling as the parameter, in figure 12. The magnitude of the thrust increases with decreasing back pressure, because the thrust is the product of the mass flow rate and the momentum of the unit mass flow rate at the nozzle exit, the reduction in the back pressure increases the adiabatic heat drop and the mass flow rate is unaffected by the back pressure. Also, as can be seen from the figure, the thrusts for nozzles E and F increase with inlet subcooling, but for nozzle B the effect of inlet subcooling is small. This tendency may be attributed to the fact that the critical mass flow rate increases and the adiabatic heat drop decreases with increasing inlet subcooling. Therefore, each factor inversely affects the absolute value of the thrust. Also, it is evident that the thrust for nozzle E is less than that for nozzle B. This may be due to the fact that the mass flow rate for nozzle E is lower than that for nozzle B, as shown in figure 12. The thrust for nozzle F is greater than that for nozzle B, since nozzle F has a larger throat diameter and the mass flow rate is greater than that for nozzle B. It should be noted that the magnitudes of the flow rates for nozzles B, E and F are different, due to the differences in the flow resistance and nozzle throat diameter. Therefore, in order to investigate the nozzle performance, the magnitude of the thrust per unit mass flow rate is discussed as follows. The measured values of the thrust per unit mass flow rate are

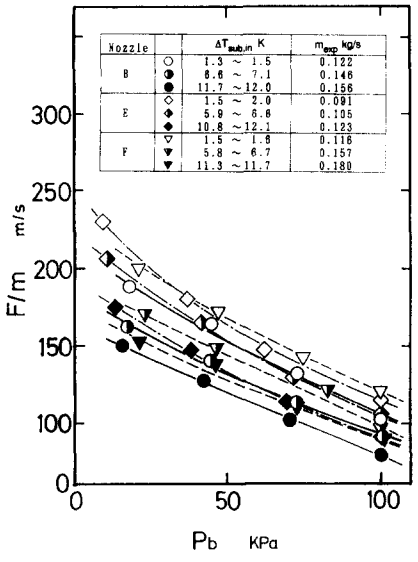

Figure 13. Thrust per unit flow rate vs back pressure.

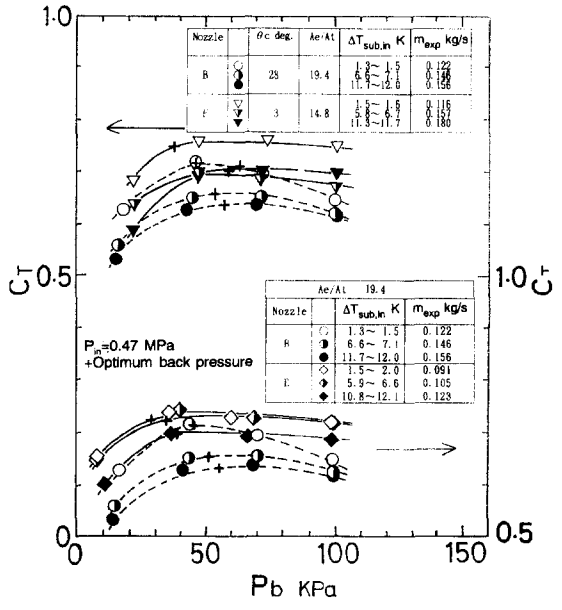

Figure 14. Thrust coefficient for the conventional and improved nozzles.

shown in figure 13. As can be seen from the figure, the thrust increases with decreasing subcooling. In addition, the thrusts for nozzles E and F have higher performance than that for nozzle B from the viewpoint of a unit mass flow rate. A comparison of nozzle performance is discussed by using the thrust coefficient defined by

$$C_T = \frac{F_{exp}}{m_{exp} W_{th}}, \qquad [6]$$

where W_{th} is the ideal velocity at the nozzle exit for the isentropic process.

3.7.1. Effect of the installation of fine wires on the thrust coefficient. The thrust coefficients for nozzles B and E are plotted against the back pressure, with inlet subcooling as the parameter, in the lower part of figure 14. As shown in this figure, the value of the thrust coefficient for nozzle E is higher than that for nozzle B, i.e. the nozzle performance is improved by the installation of the fine wires. The reason is believed to be as follows. As can be seen from figure 4, the decrease in the maximum nonequilibrium pressure drop at the nozzle throat in nozzle E results in a greater pressure difference between P_f and the exit pressure than in nozzle B. Thus, the greater pressure difference may cause the two-phase flow to accelerate in the divergent passage more than in the case of nozzle B. Next, it can be seen that the installed fine wires have a large effect on the improvement of the thrust coefficient with increasing inlet subcooling and improve the nozzle thrust coefficient by a maximum of 10%. Finally, the thrust coefficient for nozzle E takes a maximum value at and slightly above the optimum back pressure.

When the back pressure is changed, the thrust coefficient takes a maximum value. The maximum thrust coefficient is defined as C_{Tmax} in this paper. The C_{Tmax} for nozzles BS, B, BL, ES, E and EL are plotted against the exit stream-expansion ratio, i.e. A_e/A_t (a dimensionless exit cross-sectional area based on the throat), with inlet subcooling as the parameter, in the lower part of figure 15. The values of C_{Tmax} for nozzle E are 0.7–0.75, independent of A_e/A_t, and are higher than those of nozzle B. Thus, the installation of the fine wires improves the nozzle thrust coefficient in the range of $A_e/A_t = 10$ to 25 and high inlet subcooling. The maximum value of C_{Tmax} is 0.75 in these experiments.

3.7.2. Effect of the convergent angle. The thrust coefficient for nozzle F is plotted against the back pressure in the upper part of figure 14. The tendency of the thrust coefficient for nozzle F is similar to that for nozzle E. The magnitude of the thrust coefficient for nozzle F is approximately equal to that for nozzle E, in spite of the smaller maximum nonequilibrium pressure drop at the throat for nozzle F than that for nozzle E. This may be considered to be due to the higher energy

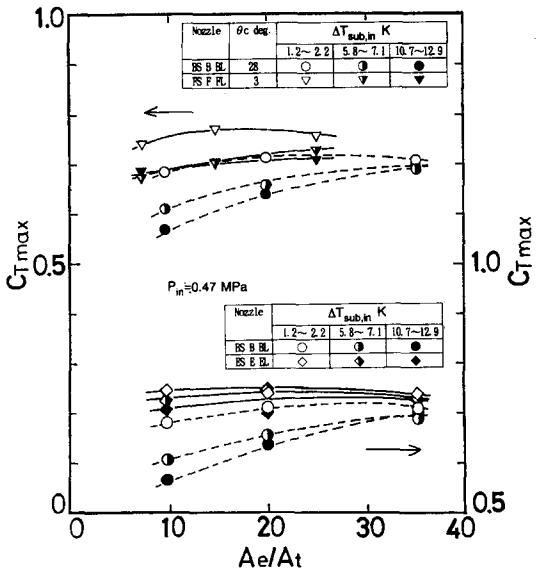

Figure 15. Maximum thrust coefficient for the conventional and improved nozzles.

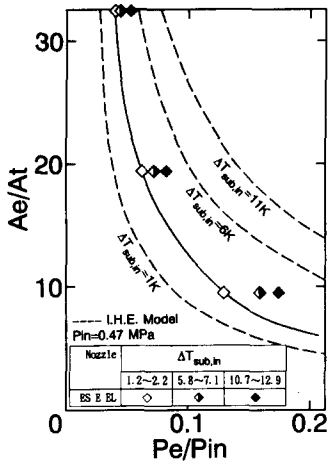

Figure 16. Relationship between the exit stream-expansion ratio and the ratio of exit to inlet pressures.

loss via friction in the long convergent passage of 0° and 3°. The values of C_{Tmax} are plotted against A_e/A_t in the upper part of figure 15. As shown in this figure, the C_{Tmax} for nozzle F is improved by 5–12% compared with nozzle B and the values of C_{Tmax} are 0.68–0.76.

3.8. Design of the exit stream-expansion ratio

A way to determine the exit stream-expansion ratio is described for a nozzle with a smaller maximum nonequilibrium pressure drop at the throat. As mentioned above in subsections 3.7.1 and 3.7.2, the thrust coefficient took maximum values at and slightly above the optimum back pressure. Thus, it could be recommended that a slightly larger exit stream-expansion ratio than that corresponding to the optimum back pressure should be selected for a given inlet condition. In figure 16 an appropriate exit stream-expansion ratio is shown on and just above the solid line. For example, in the case of an inlet pressure of 0.47 MPa, an inlet subcooling of 1 K and $P_b/P_{in} = 0.1$, we decided that values of 12 and slightly above are appropriate exit stream-expansion ratios from observing figure 16.

4. CONCLUSIONS

Experiments using 9 different nozzles were carried out for initially subcooled hot water to improve nozzle efficiency. The nozzle inlet pressure was 0.47 MPa and the inlet subcooling and back pressure were varied in the ranges 0.9–12.9 K and 5–101.3 kPa, respectively. The results are as follows:

(1) The optimum pressure profile was changed by the installation of fine wires or by decreasing the convergent angle.
(2) Decreasing the maximum nonequilibrium pressure drop at the throat improved the thrust coefficient by as much as 10%.
(3) The maximum thrust coefficient was independent of the inlet subcooling and exit stream-expansion ratio for nozzles with a small maximum nonequilibrium pressure drop at the throat.
(4) A correlation between an appropriate exit stream-expansion ratio and the ratio of the exit to inlet pressures was obtained empirically for a nozzle with a small maximum nonequilibrium pressure drop at the throat.
(5) The critical flow rate for a nozzle with a small maximum nonequilibrium pressure drop at the throat was found to be lower than that for ordinary nozzles.

REFERENCES

ABUAF, N., JONES, O. C. JR, WU, B. J. C. 1983 Critical flashing flows in nozzles with subcooled inlet conditions. *Trans. ASME Jl Heat Transfer* **105,** 379–383.

AKAGAWA, K., FUJII, T., TAKAGI, S., TAKEDA, M. & TSUJI, K. 1984 Performance of a hero's turbine using a two-phase mixture as the working fluid (experimental results in an air–water two-phase system). *Bull. JSME* **27,** 2795–2802.

AKAGAWA, K., FUJII, T., OHTA, J. & TAKAGI, S. 1988a Cycle performance of total flow turbine systems (2nd report, utilization of wet steam). *Trans. JSME* **B54,** 1509–1515 (in Japanese).

AKAGAWA, K., FUJII, T., OHTA, J., INOUE, K. & TANIGUCHI, K. 1988b Performance characteristics of convergent–divergent nozzles for subcooled hot water. *Int. J. JSME Ser. II* **31,** 718–726.

ALAMGIR, M. D. & LIENHARD, J. H. 1981 Correlation of pressure undershoot during hot-water depressurization. *Trans. ASME Jl Heat Transfer* **103,** 52–55.

ALGER, T. W. 1975 The performance of two-phase nozzles for total flow geothermal impulse turbines. Report UCRL-76417.

ALGER, T. W. 1978 Droplet phase characteristics in liquid-dominated steam–water nozzle flow. Report UCRL-52534.

ARDRON, K. H. 1978 A two-fluid flow model for critical vapour–liquid flow. *Int. J. Multiphase Flow* **4,** 323–337.

AUSTINE, A. L., HIGGINS, G. H. & HOWARD, J. H. 1973 The total flow concept of recovery from geothermal hot brine deposits. Report UCRL-51366.

COMFORT, W. J. 1977 The design and evaluation of a two-phase turbine for low quality steam–water mixtures. Report UCRL-52281.

FINCKE, J. R., COLLINS, D. R. & WILSON, M. L. 1977 The effects of grid turbulence on nonequilibrium choked nozzle flow. Report NUREG/CR-1977.

HENRY, R. E. & FAUSKE, H. K. 1971 The two-phase critical flow of one component mixtures in nozzles, orifices and short tubes. *Trans. ASME Jl Heat Transfer* **93,** 179–187.

HIJIKATA, K., MORI, Y., NAGASAKI, T. & SONODA, Y. 1985 Fundamental study on the production of high-speed mist flow by expansion of low-temperature hot water. *Trans. JSME* **B51,** 1017–1025 (in Japanese).

HOKKESON, G. 1981 Optimal two-phase flow nozzle configuration at large volume ratios. *AIAA Jl* **19,** 1547–1550.

IKEDA, T. & FUKUDA, S. 1980 A hot water turbine for waste heat recovery. *Trans. JSME* **83,** 1528–1533 (in Japanese).

ISBIN, H. S. 1980 Some observations on the status of two-phase critical flow models. *Int. J. Multiphase Flow* **6,** 131–137.

LEVY, S. 1965 Prediction of two-phase critical flow rate. *Trans. ASME Jl Heat Transfer* **87,** 134–142.

MOODY, F. J. 1966 Maximum two-phase vessel blowdown from pipe. *Trans. ASME Jl Heat Transfer* **88,** 285–295.

RICHTER, H. J. 1983 Separated two-phase flow model: application to critical two-phase flow. *Int. J. Multiphase Flow* **9,** 511–530.

SCHROCK, V. E., STARKMAN, E. S. & BROWN, R. A. 1977 Flashing flow of initially subcooled water in convergent–divergent nozzles. *Trans. ASME Jl Heat Transfer* **99,** 263–268.

WALLIS, G. B. 1980 Critical two-phase flow. *Int. J. Multiphase Flow* **6,** 97–112.

ZIMMER, G. A., WU, B. J. C., LEONHARD, W. L., ABUAF, N. & JONES, O. C. JR 1979 Pressure and void distributions in a converging–diverging nozzle with non-equilibrium water vapor generation. Report BNL-NUREG-26003.